A study of the Geogrid-Subballast Interface via Experimental Evaluation and Discrete Element Modelling

Ngoc Trung Ngo[1], Buddhima Indraratna[2], and Cholachat Rujikiatkamjorn[3]

[1]Research Fellow, School of Civil, Mining and Environmental Engineering, University of Wollongong, Wollongong City, NSW 2522, Australia; ARC Centre for Excellence for Geotechnical Science and Engineering, Australia. Email: trung@uow.edu.au, Ph: +61 2 4221 3385 Fax: +61 2 4221 3238

[2]Research Director, Distinguished Professor of Civil Engineering, Centre for Geomechanics and Railway Engineering, Faculty of Engineering, University of Wollongong, Wollongong, NSW 2522, Australia. ARC Centre for Excellence for Geotechnical Science and Engineering, Australia, Email: indra@uow.edu.au, Ph: +61 2 4221 3046 Fax: +61 2 4221 3238

[3]Associate Professor, Centre for Geomechanics and Railway Engineering, Faculty of Engineering and Information Sciences, ARC Centre of Excellence for Geotechnical Science and Engineering, University of Wollongong, Wollongong, NSW 2522, Australia. Email: cholacha@uow.edu.au, Ph: +61 2 4221 5852 Fax: +61 2 4221 3238

ABSTRACT

This paper presents a study of the interface of geogrid reinforced subballast through a series of large-scale direct shear tests and discrete element modelling. Direct shear tests were carried out for subballast with and without geogrid inclusions under varying normal stresses of σ_n = 6.7 kPa to 45 kPa. Numerical modelling with three-dimensional discrete element method (DEM) was used to study the shear behaviour of the interface of subballast reinforced by geogrids. In this study, groups of 25–50 spherical balls are clumped together in appropriate sizes to simulate angular subballast grains, while the geogrid is modelled by bonding small spheres together to form the desired grid geometry and apertures. The calculated results of the shear stress ratio versus shear strain show a good agreement with the experimental data, indicating that the DEM model can capture the interface behaviour of subballast reinforced by geogrids. A micromechanical analysis has also been carried out to examine how the contact force distributions and fabric anisotropy evolve during shearing. This study shows that the shear strength of the interface is governed by the geogrid characteristics (i.e. their geometry and opening apertures). Of the three types of geogrid tested, triaxial geogrid (triangular apertures) exhibits higher interface shear strength than the biaxial geogrids; and this is believed due to multi-directional load distribution of the triaxial geogrid.

1. Introduction

A railway track network is commonly used for transportation infrastructure worldwide due to its economic cost of construction and ease of maintenance. A track substructure consists of a

compacted layer of subballast placed above a formation soil and a coarse granular medium (ballast) placed over the subballast [1]. The functions of subballast are to transmit and distribute the wheel load from the sleepers and ballast to the formation soil at a reduced and acceptable level of stress [2, 3]. Subballast often consists of broadly graded and naturally occurring or processed mixtures of sand and gravel that is meant to prevent coarse ballast aggregates from penetrating into the subgrade and subgrade fines from migrating upwards into the ballast [4]. Under cyclic loading induced by passing trains, the granular aggregates gradually degrade and begin to lose their shear strength and drainage capacity [5-8]. Subballast also acts like a filter and a separating layer, so it must be permeable enough to avoid excess pore pressure building up under repeated loads and assist track drainage. In this layer, a geosynthetic inclusion is often employed to strengthen its mechanical properties [9, 10]. Geosynthetics are increasingly used to stabilise the substructure of rail tracks [11-15]. It is known that geosynthetics provides additional confinement for the granular layers and thus restrain the track substructure from deformation. Geogrid is a type of planar geosynthetic commonly used to provide lateral and vertical constraints to ballast and subballast aggregates; it acts like a non-horizontal displacement boundary which confines the surrounding particles through interlocking, i.e. frictional resistance between itself and the ballast aggregates [16-17].

The Discrete Element Method (DEM) introduced by Cundall and Strack [18] has been used to study the mechanical behaviour of granular materials [19-24]. Chen *et al*. [25] used DEM to simulate a box test of ballast reinforced with geogrid under confined and unconfined conditions and they reported that geogrid reinforcement can reduce ballast settlement when it is placed at an optimum location; and thus reduced the associated maintenance costs. Han *et al*. [26] used DEM to model an embankment reinforced with geogrid and stated that an embankment supported by piles and reinforced by geogrid could exhibit up to 50% less total settlement than unreinforced embankments, but these studies did not capture the irregular shape of particles accurately because only two-ball clumps or circular balls were used to model angular aggregates.

Subject to traffic loading, the subballast (capping layer) also undergoes significant lateral spreading that leads to substantial track settlement owing to insufficient confinement [9]. To strengthen the subballast layer and thereby mitigating the excessive deformation of the underlying softer subgrade (e.g. estuarine soils), the inclusion of geogrids into the subballast layer is a promising approach. There has only been limited research carried out on the effect of geogrids on subballast, where the interface behaviour of geogrid-subballast has not been studied in details either in laboratory or numerical modelling [16]. Previous studies were carried out by the Authors (i.e. Indraratna et al.[10]; Ngo et al.[21]) on fresh and coal-fouled ballast with and without inclusion of geogrids using

large-scale direct shear tests and through discrete element modelling (DEM). The results of these studies indicate that geogrid increases the shear strength and apparent angle of shearing resistance, while only slightly decreasing the vertical displacement of the composite geogrid-ballast system. However, when ballast was fouled by coal fines, the benefits of geogrid reinforcement decreased in proportion to the increasing level of fouling. Fouled ballast reinforced by geogrids was simulated in the DEM to study the influence of ballast fouling as well as the role of geogrid on the deformation and degradation of ballast in a micro-mechanical perspective. Recently, Biabani and Indraratna [16] carried out direct shear tests on subballast reinforced by geosynthetics and they confirmed that interface shear strength was governed by the normal stress, the shearing displacement rate, the relative density of the material, and the type of geosynthetics (i.e. aperture size). Results of some of these laboratory tests are used in this paper to validate the DEM model.

Most prior studies only examined soils reinforced by geosynthetics, a very few attempts have been made to study subballast reinforced by geogrids in the laboratory or via numerical modelling [27-29]. Moreover, these studies of subballast were limited by only using the continuum method (i.e. finite element or finite difference method) which means the discrete nature and angular shaped grains of subballast has not been examined properly. Despite some efforts to model granular materials reinforced with geosynthetics, the interaction mechanism and the interface behaviour between the subballast and geogrid which is governed primarily by subballast aggregates and geogrid interlocking, are not understood very well from a micromechanical perspective. It is noted that while the previous works were predominantly focused on laboratory and DEM modelling for ballast, this paper investigates the interface behaviour of geogrid reinforced sub-ballast where different types of geogrids (i.e. biaxial, triaxial geogrids) having distinctly different apertures (i.e. 37 mm to 65 mm) were examined thoroughly both in the laboratory and via DEM modelling.

2. Experimental study

2.1. Materials tested

The subballast used in this study came from Bombo quarry near Wollongong, Australia, after which it was then cleaned and sieved according to Australia Standards - AS 2758.7 [30]. The particle size distribution of the subballast used in this study is presented in Figure 1a that is similar to those commonly used in New South Wales (i.e. D_{max} = 19 mm, D_{min} = 0.075 mm, C_u = 16.3, C_c = 1.3, γ_d = 18.5 kN/m³). Fig. 1 shows several particle size distributions of subballast commonly used in railway industry worldwide. Three types of geogrids with various geometry and apertures (i.e. biaxial geogrids, BG1, BG2 and triaxial geogrid (TG3) were tested to determine how the opening

aperture and geometry affect the shear strength of the interface (Fig. 2a). The physical and mechanical characteristics of these geogrids are presented in Table 1.

2.2. Large scale direct shear test

A large scale direct shear apparatus consisting of a 300mm long ×300mm wide × 200mm high steel box divided horizontally into two equal halves was used to study the interface of geogrid-reinforced subballast in the laboratory, as shown in Fig. 2b. The subballast was placed into the shear box and compacted into several layers to achieve an approximate field unit weight of $\gamma_d = 18.5$ kN/m^3. Once the bottom half of the shear box was filled with compacted subballast, a sheet of geogrid was placed at the interface between the upper and lower boxes. The upper half of the shear box was filled with subballast and compacted to achieve the desired unit weight. Large-scale direct shear tests of subballast with and without geogrids were carried out at relatively low normal stresses which vary from $\sigma_n = 6.7$ kPa to 45 kPa to simulate actual track conditions (i.e. low confinement tracks); the subballast was then sheared to a horizontal displacement of Δh=30 mm (i.e. shear strain of $\varepsilon_s = 10\%$). During these tests, the shear force and the vertical displacements were measured at every 1mm of horizontal displacement by load cells and displacement potentiometers, respectively.

3. Numerical modelling using the Discrete Element Method

The discrete element method (DEM) was used in this study to investigate the interface of subballast reinforced with geogrid, because, the micromechanical features of granular materials and the contact force distributions that develop between particles could then be studied. The DEM enables us to accurately model the irregular shaped particles, particle breakage and the evolution of fabric anisotropy [31-36]. DEM can also examine the mechanical behaviour of a granular assembly consisting of a collection of arbitrarily shaped discrete particles subjected to quasi-static and dynamic conditions [37, 38]. In DEM, the interaction between discrete particles can be considered as a dynamic process based on a time-stepping algorithm with an explicit finite difference scheme. Particle motion was determined using Newton's second law and the interaction between particles was determined using contact laws [39], as given in the Appendix. The linear contact law was used in the current analysis where any overlap between two particles in contact generate linear forces in both normal and shear directions as governed by normal and shear stiffness coefficients k_n and k_s. Geogrids are modelled by bonding spheres together using the parallel bond model embedded in PFC3D [39] where each bond can transmit both forces and moments between spheres. It can be a set of elastic springs having constant normal and shear stiffness distributed uniformly over a circular cross section lying on the contact plane, and centered at the contact point [21].

3.1   DEM modelling of geogrids

Three types of geogrids (biaxial and triaxial grids), which are identical to those used in the laboratory, were simulated in the current analysis. A biaxial geogrid with 40 mm × 40 mm (BG1) apertures was modelled by bonding a number of small spheres together (i.e. 13,248 spheres of 1.5 - 3 mm in diameter), as shown in Fig. 3a. The geogrid consists of different size spheres to simulate the actual geometry where the larger balls were used to model the geogrid junctions, and the smaller balls at the centre of the ribs. This geogrid has 28 square apertures, similar to the geogrid used in the laboratory. The spheres were connected by parallel bonds which correspond to the tensile strength of the geogrid (i.e. within the elastic range), as determined by the tensile tests. Each bond presents the load and displacement of a finite sized piece of cementitious material deposited between two spheres in contact which transmits forces and a moment [39]. A similar approach was used to model another biaxial geogrid BG2 (aperture 65 mm × 65 mm) and a triaxial grid TG3 (the largest aperture is 37 mm). A total of 7170 and 15,804 spheres were required to model BG2 and TG3, respectively (Figs. 3b-c). Previous studies conducted by the Authors [6, 21] simplified the modelling of the geogrid's geometry by connecting a series of single spheres together, i.e. spheres of 2 mm radius at a rib and 4 mm radius at the junction. This simplification could lead to buckling of simulated geogrids (i.e. in the vertical direction) that was not actually observed in the laboratory tests. The current DEM analysis models the geogrids in a more realistic manner where the geometry of the ribs and junctions of different geogrids were modelled accurately, mimicking actual geogrid's size and shape. In addition, the triaxial geogrid having triangular structure, coupled with improved rib and junction geometry, was also investigated. A large number of spheres having different sizes were required to simulate realistic shape for geogrids to provide better mechanical interlocking with particles, albeit increased computational time [40].

Determining the model parameters for geogrids (i.e. stiffness, parallel bond strength, friction coefficient, etc.) can be complex due to the large number of parameters required, such as the stiffness k_n and k_s, the coefficient of friction f, and the parameters for bonding which control the flexibility and strength of geogrids. The micromechanical parameters needed in this study to model geogrids were determined by back calculating the load-displacement responses with the laboratory test results of tensile tests (following the ASTM D4885 Standards [41]), as shown in Fig. 4. Tensile tests with varying normal and shear parallel bond stiffness were simulated in DEM; and the optimum matching between the tensile force-strain data obtained from the simulations and the results measured in the laboratory is presented in Fig. 4c. It is noted that one cannot expect to identify all parameters uniquely from a given test, in this study the micromechanical properties

were selected based on tensile test results assuming that the normal stiffness along a rib and between a rib and junction are the same. During the calibration process, it was necessary to adjust the mechanical parameters of the parallel bond (i.e. contact and shear stiffness, k_n, k_s, friction coefficient, μ, bond strength, etc.) until we could obtain a reasonable agreement between the DEM simulations and the laboratory data. The most appropriately calibrated DEM parameters were then determined accordingly, as given in Table 2. This approach has been used earlier by McDowell et al. [19]; Ngo et al. [21], among others. Although the tensile test is effective for characterizing the grid, further tests (i.e. single-junction test, the in-plane rotation test) are necessary for more comprehensive characterization, and thus future work involving DEM will facilitate more accurate modelling of the geogrid stabilized granular media. It is noted that laboratory tests observed very little bucking of the geogrids caused by sharp and angular subballast particles during the sample preparation and shearing process. The current DEM analysis does not consider the influence of the geogrid bucking and this is a limitation of the current study.

3.2   DEM modelling of geogrid-subballast interface

This section provides the description of the experimental set up for the purpose of simulating the direct shear test process in DEM. Irregular grains of subballast with different shapes and sizes were simulated in DEM by clumping a number of spheres together at appropriate sizes and positions to mimic the actual shapes and gradation of subballast [34]. A library of nine particles of subballast was then generated by overlapping 25 to 50 spheres together using clump logic [39], as shown in Fig. 5a. This approach has been previously used by Ferellec and McDowell [40]. These particles range from 2.5 mm to 19 mm and represent the particle size distribution carried out in the laboratory. Smaller particles were not considered in this analysis to avoid excessive computational time. Lim and McDowell [42]; and Ngo *et al*. [43] also used this approach to model granular materials, and reported that the absence of small-sized particles (i.e. less than 2 mm) has no pronounced effect on the results as long as the relative density of the samples is similar to those in the laboratory. Subballast is significantly smaller than ballast aggregates and thereby requiring smaller-sized spheres to adequately simulate the actual angularity of these aggregates. It is noted that the surface of actual subballast is also rough and presents irregularities and sharpness, thereby if fewer particles are used, the simulated subballast would be more rounded and less angular. Considering the computational efficiency, the Authors have observed that using 25 to 50 spheres to model subballast, the simulation could still be completed in a reasonable time (less than 200 hours for one simulation, running on a Workstation, Dell Precision T1700, RAM: 64 GB).

DEM models for large-scale direct shear tests were used to model geogrid-reinforced subballast where the simulated geogrid is positioned in the middle of the apparatus, as shown in Fig. 5b. Large-scale shear apparatus (300mm long ×300mm wide × 200mm high), divided horizontally into two equal compartments, was simulated with rigid walls. A loading plate was placed on the top boundary of the apparatus to allow the subballast sample to displace vertically during shearing. This plate was also used to apply a normal stress to the sample and to measure vertical displacement (i.e. normal strain) during shearing. Irregular shaped particles of subballast were generated by 'clumping,' as stated earlier, using the sub-routines developed by the Authors. Simulated particles of subballast were placed at random locations within the specified boundaries of the shear box and without overlapping, and then compacted to a unit weight of $\gamma_d = 18.5$ kN/m³ (i.e. this is identical to the unit weight of subballast carried out in the laboratory). A simulated geogrid was then placed in the middle of the shear box and secured to the boundary walls. To prevent the geogrid from being damaged during installation, two temporary rigid walls were placed above and below the geogrid (i.e. to separate the geogrid and the subballast particles). Once the geogrid was securely placed in the middle of the shear box, the temporary walls were removed and the geogrid was allowed to interact freely with the surrounding grains. A normal force applied on top of the shear box was kept constant by adjusting the position and velocity of the top loading plate using a numerical servo-control.

Several micromechanical parameters are required to simulate a specific material in DEM. It was found that the friction coefficient (μ) and normal and shear contact stiffness of particle contacts (k_n and k_s) are generally considered as predominant parameters governing the stress-strain behavior of the material. Their determination requires different experiments in which each parameter or group of parameters varies independently. In the current analysis, a series of direct shear tests for subballast were simulated where the contact stiffness and inter-particle coefficients of friction were selected in such a way, until the calculated shear stress ratio versus shear strain could be matched reasonably well with the laboratory data. Fig. 6 shows a comparison of the shear stress and displacement of subballast with varying values of μ; this indicates that $\mu = 0.85$ provides the most appropriate calibration with the test data. A set of micromechanical parameters selected to model subballast in the current analysis is then shown in Table 3.

The lower part of the shear box was sheared horizontally at a velocity of 8.35×10^{-5} mm/s to a horizontal displacement of $\Delta h= 30$ mm, while the upper part of the shear box was fixed. Simulations of direct shear tests were carried out for reinforced and unreinforced subballast specimens subjected to varying normal stresses of $\sigma_n = 6.7 - 45$ kPa; this was similar to those

carried out in the laboratory. During the shearing process, the shear forces and the corresponding shear strain were recorded at every 1mm of horizontal displacement.

4. Results and discussion

4.1 Shear stress-strain analysis

DEM simulations of large-scale direct shear tests for unreinforced subballast were carried out under three normal stresses of $\sigma_n = 6.7, 20.5,$ and 45 kPa. In these simulations, the bottom part of the shear box was loaded in a strain-controlled mode by specifying the velocity of the bottom walls (i.e. 8.35×10^{-5} mm/s). During this shearing process, the top boundary moved vertically because the loading platens were under a stress-controlled condition. The shear stress ratio τ/σ_n and the normal strain ε_n (i.e. the vertical displacement) at a corresponding shear strain of ε_s, as obtained from DEM analysis and then compared to the laboratory data, are presented in Fig. 7. Note that the results obtained from DEM simulations agree reasonably well with the experimental data at a given normal stress, showing that the set of micromechanical parameters (Table 3) adopted in the analysis is appropriate. The strain softening behaviour of subballast and its volumetric dilation were observed in all simulations and revealed that the greater the normal stress (σ_n), the lower the shear stress ratio, τ/σ_n and the smaller the dilation would be. It is noted that the calibration of the micromechanical parameters for subballast was conducted under a given normal stress of 35 kPa (Fig. 6), while the simulations of laboratory tests were carried out under three normal stresses of σ_n = 6.7, 20.5, and 45 kPa. Although the same coefficient of friction, $\mu = 0.85$ was used for these simulations, the stress ratio obtained varied considerably from 0.9 to 1.35; where a lower normal stress was applied, a higher stress ratio was observed, as expected. It is also noted that the shear stress ratio (i.e. normalized shear strength) of granular materials measured in direct shear tests depends on several factors including the applied normal stress, friction coefficient, shearing rate, and boundary conditions among others.

DEM simulations were used to model subballast reinforced by three types of geogrids (BG1, BG2, and TG3) subjected to a relatively small normal stress of 6.7 kPa (i.e. representing low confinement in actual tracks). Figure 8 shows a comparison of the shear stress ratio and the normal strain versus the shear strain obtained by DEM with the laboratory data. Here, the calculated shear stress ratio and normal strain versus shear strain curves generally agree with the experimental data. Triaxial geogrid (TG3) had the highest ratio of τ/σ_n, while the biaxial geogrid (BG2) had the smallest shear stress ratio and the highest rate of dilation. The specimen of subballast with triaxial geogrid

inclusion also experienced the lowest volumetric dilation because it is believed that the triangular geometry of the triaxial geogrid, distributes the stress more uniformly across the geogrid and can provide better interlock with aggregates than the square apertures of the biaxial grids. This improved performance from triaxial geogrid may also be attributed to the isotropic radial stiffness of TG3, which is almost consistent in every direction, and which confines the grains of subballast better at their interfaces.

It is noted that the granular materials (i.e. ballast aggregates) having a large mean particle size (i.e. $d_{50} > 35$ mm) commonly show scattering of data both in laboratory tests and DEM simulations, as observed by the Authors' previous studies on ballast [e.g. 10, 21]. It is noteworthy that the particle size of subballast conducted in this study (i.e. $d_{max}= 19$ mm, $d_{50} =3.3$mm) is much smaller than median ballast grain size (i.e. $d_{50}=38$ mm), and the results are presented in a normalized stress ratio (i.e. τ/σ_n), thereby now showing reduced scattering of measured data. In addition, extensive laboratory tests were also carried out to examine the influence of relative density and the rate of shearing displacement on the shear strength of subballast to examine influence of initial conditions and repeatability of experimental results. Results of these tests confirmed that at a lower relative density, only marginal improvement in performance was observed for reinforced sub-ballast compared to the unreinforced specimen. By increasing the relative density (i.e. $D_R=40\% - 77\%$), the performance could be improved substantially. However, by further increasing the relative density from 77% to 85%, only a marginal improvement was observed in the reinforced subballast. Based on these results, a relative density of about 77% was selected as the optimum density to provide acceptable interface resistance between the subballast and the geogrid.

4.2   Performance of the geogrids based on DEM

Figure 9 shows the distributions of average contact forces with the depth of shear box for unreinforced and geogrid-reinforced subballast assemblies at a shear strain of $\varepsilon_s = 5\%$ and a normal stress of $\sigma_n = 6.7$ kPa. Here the unreinforced subballast exhibits the least developed contact forces, unlike the reinforced assemblies. Subballast reinforced by the triaxial geogrid (TG3) has the highest mobilised contact forces at the interface (i.e. approximately 71N for TG3 compared to 53N and 39N for BG1 and BG2, respectively). There is a confinement zone of around 50 mm from the geogrid-subballast interfaces where the inclusion of geogrid leads to a significant increase in the contact forces. In fact, the average contact forces at the interface were approximately three times greater than at the top and bottom of the shear box. This mobilisation of large contact forces within the confinement zone of geogrids stems from the strong mechanical interlock between the geogrid and subballast aggregates [10, 21].

Figure 10 shows the contour strains that developed across the geogrids in the direction of horizontal shearing (ε_{xx}) for biaxial and triaxial geogrids (BG1 and TG3), when measured at a shear strain of $\varepsilon_s = 5\%$ (i.e. approximately at a peak mobilised shear strength). Note that these strains developed non-uniformly across the geogrids where the mobilised strain would be dependent on the interlock between the geogrid and subballast grains. The triaxial geogrid (TG3) has slightly smaller mobilised strains than the biaxial geogrid, BG1 (i.e. 1.0% strain for TG3 compared to 1.1% strain for BG1). In addition, the averaged strain over the whole area of the biaxial and triaxial geogrids, and they are 0.387% and 0.352%, respectively. This would be attributed to the multi-directional load distribution of triaxial geogrid which could distribute the stress more uniformly across the geogrid; and thereby decreased maximum mobilised strains.

4.3 Micromechanical analysis

Granular grains subjected to shear loading can induce changes in the contact forces and subsequent changes in the number of load carrying contacts and their orientations; the load is transmitted to subballast grains through an interconnecting network of force chains at contact points [44, 45]. A fabric tensor is often used as an index to capture the packing structure of granular materials where the macroscopic stress and strain can be related to microscopic force and fabric parameters (i.e. the stress-force-fabric relationship). The stress and strain relationship for a granular assembly can be computed by integrating the inter-particle contacts using a micro-macro relationship. The micromechanical analysis presented here focuses on the changes of fabric and contact force orientations representing the transmission of the load applied to the grains which occurs during shearing, as described in the Appendix.

Figure 11 shows the evolution of fabric tensor components: F_{11}, F_{22}, and F_{33} (determined by Equation 6 in the Appendix) of unreinforced and geogrid-reinforced subballast assemblies during shearing, where it can be seen that the fabric components change significantly as shearing progresses. The unreinforced subballast assembly has more variations of fabric indices than the reinforced assemblies where all the fabric components increased from the beginning of shearing up to around 5% shear strain, and then began to decrease. This reduction in the changes of fabric indices associated with the inclusion of geogrids is believed to be due to interlocking between the subballast and geogrid, which inhibits the particles from becoming displaced. In fact, this increase in contact at the initial stage of shearing indicates that the particles are being rearranged and rotated to support the induced loads. The reinforced assembly shows relatively consistent values of fabric components and the F_{ii} varies from approximately 0.32 to 0.34. The principal vector, F_{11} is determined in the vertical direction whereas the other two principal vectors, F_{22}, F_{33} are determined

in the horizontal directions based on Cartesian coordinates. The fabric component F_{11} has the highest value for all specimens which indicate that the fabric contact is predominately in a vertical direction. Moreover, all the fabric components F_{ii} for the triaxial geogrid reinforced subballast remain close together as shearing progresses (Fig. 11d), while the biaxial geogrid, BG2 (Fig. 11c) has greater variations.

Figure 12 shows polar histograms of contact orientations for unreinforced and reinforced subballast at different shear strains, which vary from $\varepsilon_s = 0$ to 10% when subjected to a normal stress of $\sigma_n = 6.7$ kPa. A polar histogram of contact forces was obtained by collecting the contact force at a specified bin angle of $\Delta\theta_i = 10^0$ projected onto a vertical plane, while the corresponding number of contacts in that bin are determined by $\Delta N_c(\theta_i)$. At the beginning of the tests ($\varepsilon_s = 0$), the normal contact force anisotropy for the unreinforced and reinforced assemblies is approximately coaxial, with vertical axes having a principal direction of around $\theta_r = 7^0$, 8^0, and 12^0 (Figs. 12a, 12d, 12g) for the unreinforced and reinforced assemblies with BG1 and TG3, respectively. It is noted that the dominant direction of contact forces is commonly in the vertical direction. In the current DEM analysis, after generating subballast particles and geogrids inside the direct shear box, considerably high locked-in stresses induced within the subballast assemblies were observed using a measurement sphere approach, as described in the Appendix (i.e. using computation of the stress tensor). It should be noted that the process of placing particles to achieve a given unit weight generates relatively large forces and hence they should be brought to an initial at-rest condition. The subballast assembly was then cycled to reach equilibrium (i.e. reduced locked-in stresses) through facilitating particles to form contact with each other while keeping the unit weight of the assembly constant. This is believed to cause the rotation of the dominant direction of contact forces before starting the shearing process (i.e. $\Theta_r = 7^0$). This approach has also been previously used by Lim and McDowell [42], among others. An increase in the shear strain and the corresponding increase in horizontal shear displacement would facilitate particle rearrangement which leads to a redistribution of stresses and reorientation of the contact forces. As shearing progresses, contact force chains develop to resist shear and disperse the applied shear loads across the particles in the assembly resulting in contact force direction and magnitude change from a vertical to a horizontal orientation. The principal direction of contact forces grows and rotates vigorously with increased shear strains; at the end of the shear tests they reached values of $\theta_r = 26^0$, 32^0 and 41^0 for unreinforced and reinforced assemblies, respectively (Figs. 12c, 12f, 12i). This observation could be justified by an increased number of contact forces in the horizontal direction attributed to the inclusion of geogrids, and as a result, the contact forces are aligned towards the horizontal direction. It is also noted that the triaxial geogrid required more spheres than the biaxial geogrid to simulate its geometry.

However, the number of spheres does not significantly influence the principal direction Θ_r. Indeed, the direction of contact forces Θ_r of triaxial geogrid that is slightly greater than the biaxial geogrid is mainly attributed to the multi-symmetrical geometry (triangular apertures) that could distribute forces more uniformly across the triaxial grid, thereby facilitating more effective contacts in the horizontal direction.

5.   Conclusions

A series of large-scale direct shear tests have been carried out on subballast with and without geogrid inclusion, and the test data was used to validate the DEM models. Irregular particles of subballast were simulated by clumping 25-50 circular spheres together to represent an appropriate angularity. DEM models for geogrids with different geometry and apertures were developed by bonding many small spheres together with parallel bonds. Appropriate sets of micromechanical parameters to simulate subballast and geogrids were determined by back-calculating with the laboratory data. Once the micromechanical parameters had been validated properly they were used to simulate the tests of geogrid-reinforced subballast subjected to direct shear loading.

The results of the shear stress ratio versus shear strain obtained from DEM simulations were comparable to experimental data, indicating that the DEM model proposed in this study could adequately capture the interface behaviour of subballast reinforced with geogrids. Laboratory and numerical modelling data confirmed that the shear strength of the reinforced subballast assembly increased with the inclusion of geogrids, although the improved shear strength depended on the opening aperture and geometry of the geogrids. Triaxial geogrid (TG3) provided the highest ratio of τ/σ_n and the lowest volumetric dilation; and this was believed due to its multi-symmetrical geometry (triangular apertures) which could distribute the stress more uniformly across the geogrid thereby sustaining more effective interlock with the grains. Distributions of average contact forces with the depth of shear box for unreinforced and geogrid-reinforced subballast assemblies were also presented, and the triaxial geogrid-reinforced subballast had the highest mobilised contact forces at the interface. Contour strains developed across the geogrids in a horizontal shearing direction were also captured, and they revealed that the strains developed non-uniformly across the geogrid and that the triaxial grid had smaller mobilised strain than the biaxial grid.

The evolution of the fabric tensor components F_{11}, F_{22}, and F_{33} of unreinforced and geogrid-reinforced subballast assemblies during shearing was analysed, and it showed that the unreinforced subballast assembly had more variations in fabric than the reinforced assemblies. Changes in the contact fabric during shearing indicates that the particles were being rearranged and rotated to

support the induced loads; once again the triaxial-reinforced subballast exhibited the least variations in the fabric tensor components (F_{ii}). A histogram of contact orientations for unreinforced and reinforced subballast at different shear strains was captured. As shearing progresses, the contact forces redistributed and reorientated; and they tended to align towards the horizontal direction of shearing to support the induced shear loads.

6. Acknowledgements

7.   Appendix: Mathematical framework of DEM modelling

At a given time, the force vector $\vec{F}$ that represents the interaction between two particles is resolved into normal ($\vec{F}_N$) and the shear component ($\vec{F}_T$) with respect to the contact plane [39]:

$$\vec{F}_N = K_N U^n \tag{1}$$

$$\delta\vec{F}_T = -K_T \cdot \delta U^s \tag{2}$$

Where, K_N and K_T are normal and tangential stiffness at the point of contact; U^n is the normal penetration between two particles (Fig. 13a); δU^s is the incremental tangential displacement; and $\delta\vec{F}_T$ is the incremental tangential force. The new shear contact force is determined by summing the old shear force at the start of the time-step with the increment of elastic shear force.

$$\vec{F}_T \leftarrow \vec{F}_T + \delta\vec{F}_T \leq \mu\,\vec{F}_N \tag{3}$$

where, μ is the coefficient of friction.

Shear stresses in a given volume V are calculated by the summation of discrete contact forces as:

$$\sigma_{ij} = \left(\frac{1-n}{\Sigma_{N_p} V}\right) \Sigma_{N_p} \Sigma_{N_c} \left| x_i^{[c]} - x_i^{[p]} \right| n_i^{(c,p)} f_j^{(c)} \tag{4}$$

where N_p, N_c are the number of particles and the number of contacts of these particles, respectively; n is the porosity within the given volume; $x_i^{[p]}$ and $x_i^{[c]}$ are the positions of a particle centroid and its contact, respectively; $n_i^{(c,p)}$ is the unit normal vector; and $f_j^{(c)}$ is the force acting at contact (c) arising from a particle.

Contact forces are characterised by the probability density distribution of inter-particle contact orientation $\overline{E}(\Omega)$ proposed by Ouadfel and Rothernburg [46] as:

$$\overline{E}(\Omega) = \frac{1}{4\pi}\left[1 + F_{ij} n_i n_j\right] \tag{5}$$

where, F_{ij} is a second order fabric tensor which represents the distribution of contact orientations in the volume of interest, and is determined by:

$$F_{ij} = \frac{1}{N_c}\Sigma_{k=1}^{N_c} n_i^k n_j^k \tag{6}$$

Note that F_{ij} is symmetrical (i.e. $F_{ij} = F_{ji}$) with the three principal values F_{11}, F_{22}, F_{33} where their sum is unity; n_i^k is a unit vector representing the orientation of the k contact (Fig. 13b); and the components of a unit vector are $(cos\gamma, \sin\gamma\cos\beta, \sin\gamma\sin\beta)$. The probability density function of all contacts satisfies:

$$\int_0^{2\pi}\int_0^{\pi} E(\Omega)\,sin\gamma\,d\gamma\,d\beta = 1 \tag{7}$$

The principal direction of contact forces, θ_r can be described by the following Fourier series approximation introduced by Rothenburg and Bathurst [47], as given below:

$$E(\theta) = \frac{1}{2\pi}[1 + a^r cos2(\theta - \theta_r)] \tag{8}$$

where, a^r and θ_r are coefficients of anisotropy of contact and the corresponding major principal directions, respectively. By comparing the contact force orientations obtained in DEM simulations with those determined by Equations 8, the principal direction of contact forces, θ_r can then be estimated at a given shear strain during the DEM analysis.

8. References

1. Selig, E.T., Waters, J.M.: Track geotechnology and substructure management, Thomas Telford, London (1994)

2. Indraratna, B., Ngo, N.T., Rujikiatkamjorn, C.: Deformation of coal fouled ballast stabilized with geogrid under cyclic load. J Geotech Geoenviron Eng. **139**(8), 1275-1289 (2013)

3. Suiker, A.S., Selig, E.T., Frenkel, R.: Static and cyclic triaxial testing of ballast and subballast. J Geotech Geoenviron Eng. **131**(6): 771–782 (2005)

4. Trani, L.D., Indraratna, B.: Assessment of subballast filtration under cyclic loading. J Geotech Geoenviron Eng. **136**(11): 1519-1528 (2010)

5. Tutumluer, E., Schmidt, S., Qamhia, I., Basye, C., Li. D., Douglas, S.C.: Ballast properties and degradation trends affecting strength, deformation and in-track performance. In: Proceedings of the AREMA 2015 Annual Conference in conjunction with the Railway Interchange, Minneapolis, MN (2015)

6. Ngo, N.T., Indraratna, B., Rujikiatkamjorn, C.: Modelling geogrid-reinforced railway ballast using the discrete element method. Transp Geotech. **8**(2016), 86-102 (2016)

7. Lekarp, F., Dawson, A.: Modelling permanent deformation behaviour of unbound granular materials. Constr Build Mater. **12**(1), 9-18 (1998)

8. Werkmeister, S., Dawson, A., Wellner, F.: Pavement design model for unbound granular materials. Journal of Transportation Engineering. **130**(5), 665-674 (2004)

9. Indraratna, B., Salim, W., Rujikiatkamjorn, C.: Advanced rail geotechnology - ballasted track, CRC Press, Taylor & Francis Group, London, UK (2011)

10. Indraratna, B., Ngo, N.T., Rujikiatkamjorn, C.: Behavior of geogrid-reinforced ballast under various levels of fouling. Geotext Geomembr. **29**(3), 313-322 (2011)

11. Bathurst, R.J., Raymond, G.P. (1987).: Geogrid reinforcement of ballasted track. Transport Res Rec. **1153,** 8-14 (2011)

12. Fernandes, G., Palmeira, E.M., Gomes, R.C.: Performance of geosynthetic-reinforced alternative sub-ballast material in a railway track. Geosynth Int. **15**(5), 311-321 (2008)

13. Pokharel, S.K., Han, J., Leshchinsky, D., Parsons, R.L., Halahmi, I.: Investigation of factors influencing behavior of single geocell-reinforced bases under static loading. Geotext Geomembr. **28**(6), 570-578 (2010)

14. Ngo, N.T. and Indraratna, B.: Improved performance of rail track substructure using synthetic inclusions: Experimental and numerical investigations." Int J Geosynth and Ground Eng, **2**(3), 1-16 (2016)

15. Biabani, M., Indraratna, B., Ngo, N.T.: Modelling of geocell-reinforced subballast subjected to cyclic loading. Geotext Geomembr. **44** (4), 489-503 (2016)

16. Biabani, M., Indraratna, B.: An evaluation of the interface behaviour of rail subballast stabilised with geogrids and geomembranes. Geotext Geomembr. **43**(3), 240-249 (2015)

17. Rujikiatkamjorn, C., Indraratna, B., Ngo, N.T., Coop, M.: A laboratory study of railway ballast behaviour under various fouling degree. In: Proceedings of the 5th Asian Regional Conference on Geosynthetics. (2012)

18. Cundall, P.A., Strack, O.D.L.: A discrete numerical model for granular assemblies". Géotechnique. **29**(1), 47-65 (1979)

19. McDowell, G.R., Harireche, O., Konietzky, H., Brown, S.F., Thom, N.H.: Discrete element modelling of geogrid-reinforced aggregates. Proceedings of the ICE - Geotech Eng. **159**(1), 35-48 (2006)

20. Tutumluer, E., Huang, H., and Bian, X.: Geogrid-aggregate interlock mechanism investigated through aggregate imaging-based discrete element modeling approach. Int J Geomech. **12**(4), 391–398 (2012)

21. Ngo, N.T., Indraratna, B., Rujikiatkamjorn, C.: DEM simulation of the behaviour of geogrid stabilised ballast fouled with coal. Comput Geotech. **55**, 224-231 (2014)

22. Powrie, W., Ni, Q., Harkness, R.M., Zhang, X.: Numerical modelling of plane strain tests on sands using a particulate approach. Geotechnique. **55**(4), 297-306 (2005)

23. Powrie, W., Yang, L.A. and Clayton, C.I.: Stress changes in the ground below ballasted railway track during train passage. J of Rail and Rapid Transit. 247-261 (2007)

24. Harkness, J., Zervos, A., Le Pen, L., Aingaran, S., Powrie, W.: Discrete element simulation of railway ballast: modelling cell pressure effects in triaxial tests. Granul Matter. **18**(3), 65 (2016)

25. Chen, C., McDowell, G.R., Thom, N.H.: Discrete element modelling of cyclic loads of geogrid-reinforced ballast under confined and unconfined conditions. Geotext Geomembr. **35**, 76-86 (2012)

26. Han, J., Bhandari, A., Wang, F.: DEM analysis of stresses and deformations of geogrid-reinforced embankments over piles. Int J Geomech. **12**(4), 340–350 (2011)

27. Sieira, A.C., Gerscovich, D.M., Sayão, A.: Displacement and load transfer mechanisms of geogrids under pullout condition. Geotextiles and Geomembranes. **27**, 241-253 (2009)

28. Aursudkij, B., McDowell, G.R., Collop, A.C.: Cyclic loading of railway ballast under triaxial conditions and in a railway test facility. Granul Matter. **11**, 391–401 (2009)

29. Biabani, M., Ngo, N.T., Indraratna, B.: Performance evaluation of railway subballast stabilised with geocell based on pull-out testing. Geotext Geomembr.. **44**(4), 579-591 (2016)

30. Australian Standard.: Aggregates and rock for engineering purposes; Part 7: Railway ballast. AS 2758.7. Sydney, Australia (1996)

31. McDowell, G. R., Harireche, O.: Discrete element modelling of soil particle fracture. Géotechnique. **52**(2), 131-135 (2002)

32. Lobo-Guerrero, S., Vallejo, L.E.: Discrete element method analysis of railtrack ballast degradation during cyclic loading. Granul Matter. **8**(3-4), 195-204 (2006)

33. Cui, L., O'Sullivan, C.: Exploring the macro- and micro-scale response of an idealised granular material in the direct shear apparatus. Géotechnique, **56**(7), 455-468 (2006)

34. Indraratna, B., Ngo, N.T, Rujikiatkamjorn, C., Vinod, J.: Behavior of fresh and fouled railway ballast subjected to direct shear testing: Discrete element simulation. Int J Geomech. **14**(1), 34-44 (2014)

35. Indraratna, B., Ngo, N.T., Rujikiatkamjorn, C., Sloan, S.W.: Coupled discrete element–finite difference method for analysing the load-deformation behaviour of a single stone column in soft soil. Comput Geotech. **63**, 267-278 (2015)

36. Ngo, N.T, Indraratna, B., Rujikiatkamjorn, C.: Micromechanics-based investigation of fouled ballast using large-scale triaxial tests and discrete element modeling. J Geotech Geoenviron Eng. (2016) doi: 10.1061/(ASCE)GT.1943-5606.0001587, 04016089

37. Lu, M., McDowell, G.R.: The importance of modelling ballast particle shape in the discrete elememt method. Granul Matter. **9**(1-2), 69-80 (2007)

38. Hu, M., O'Sullivan, C., Jardine, R.R., Jiang, M.: Stress-induced anisotropy in sand under cyclic loading. Granul Matter. **12**, 469-476 (2010)

39. Itasca.: Particle flow code in three dimensions (PFC3D) - manual. Itasca Consulting Group, Inc., Minnesota, USA. (2014)

40. Ferellec, J.F. and McDowell, G.R. (2010).: A method to model realistic particle shape and inertia in DEM. Granul Matter, 12(5), 459-467 (2010)

41. ASTM.: Standard test method for determining performance strength of geomembranes by the wide strip tensile method. D4885-01(2011). West Conshohocken, PA. (2011)

42. Lim, W.L., McDowell, G.R.: Discrete element modelling of railway ballast. Granul Matter. **7**(1), 19-29 (2005)

43. Ngo, N.T., Indraratna, B., Rujikiatkamjorn, C., Biabani, M.M.: Experimental and discrete element modeling of geocell-stabilized subballast subjected to cyclic loading. J Geotech Geoenviron Eng. **142**(4), 04015100 (2016)

44. Oda, M., Iwashita, K.: Mechanics of granular materials: An introduction, Rotterdam: A. A. Balkema. (1999)

45. D'Addetta, G.A., Ramm, E.: A microstructure-based simulation environment on the basis of an interface enhanced particle model. Granul Matter. **8**, 159–174 (2006)

46. Ouadfel H., Rothenburg L.: Stress-force-fabric relationship for assemblies of ellipsoids. Mech Mater. **33**, 201–221 (2001)

47. Rothenburg, L., and Bathurst, R.J.: Analytical study of induced anisotropy in idealized granular materials. Geotechnique. **39**(4): 601-614 (1989)

Table 1 Properties and technical specifications of geosynthetics used for tests

Geosynthetic type	BG1	BG2	TG3
Material	Polypropylene (PP)	PP	PP
Structure	Biaxial	Biaxial	Triaxial
Open area(%)	78.9	84.01	65.74
A/D_{50}	11.21	19.54	10.90
Aperture shape	Square	Rectangle	Triangle
Aperture size (mm)	40×40	65×65	37
Rib thickness (mm) (MD/CMD)	2.2[a] /1.3[a]	2.3[a] /1.3[a]	2[a] /2[a]
Tensile strength at 5% strain (kN/m)	16.5	17.5	11
Ultimate strength (kN/m) (MD/CMD)	30[b] /30[b]	30[b] /30[b]	19[b] /19[b]

[a]ASTM 4885.

[b]ASTM 6337.

Table 2 Micromechanical parameters used to model geogrids

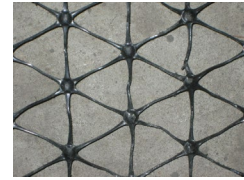| Parameter	Selected value
Particle density (kg/m^3)	972
Coefficient of friction	0.47
Contact normal stiffness, k_n (N/m)	5.91×10^6
Contact shear stiffness, k_s (N/m)	5.91×10^6
Contact normal stiffness of wall-particle, $k_{n\text{-}wall}$ (N/m)	3.25×10^9
Shear stiffness of wall of wall-particle, $k_{s\text{-}wall}$ (N/m)	3.25×10^9
Parameter of contact bond normal strength, ϕ_n (kN)	56.8
Parameter of contact bond shear strength, ϕ_s (kN)	56.8
Parallel bond radius multiplier, r_p	0.5
Parallel bond normal stiffness, k_{np} (kPa/m)	6.27×10^7
Parallel bond shear stiffness, k_{sp} (kPa/m)	6.27×10^7
Parallel bond normal strength, σ_{np} (MPa)	297
Parallel bond shear strength, σ_{sp} (MPa)	297

Table 3 Micromechanical parameters used to simulate subballast

Parameters	Value
Particle density (kg/m^3)	2350
Inter-particle coefficient of friction, μ	0.85
Contact normal stiffness, k_n (N/m)	4.82×10^8
Contact shear stiffness, k_s (N/m)	2.41×10^8
Contact normal stiffness of wall-particle, $k_{n\text{-}wall}$ (N/m)	3.25×10^9
Shear stiffness of wall of wall-particle, $k_{s\text{-}wall}$ (N/m)	3.25×10^9
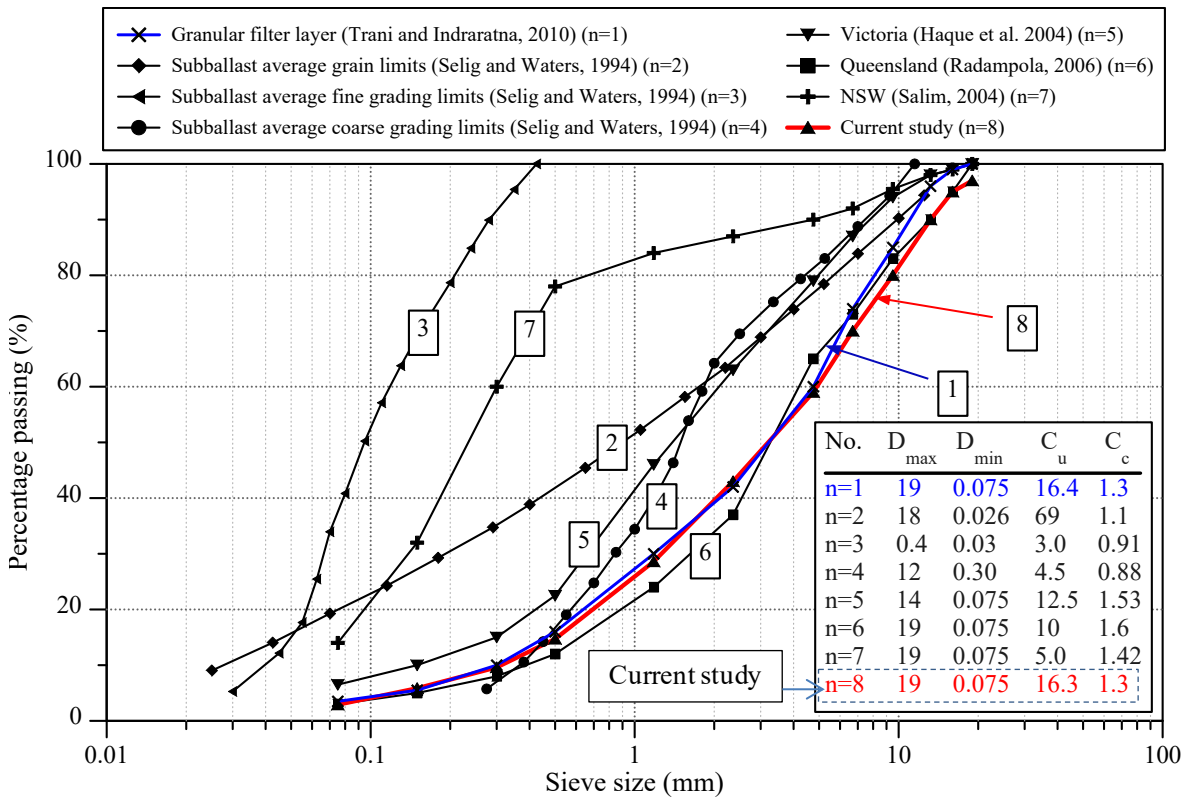
Fig 1 Particle size distribution of tested subballast compared with typical grain size gradations used in tracks
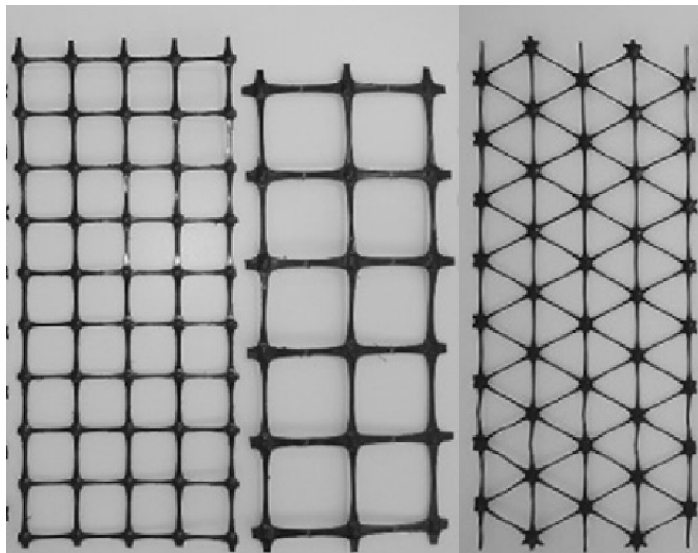
BG1
(40 x 40 mm)

BG2
(65 x 65 mm)

TG3
(Aperture = 37 mm)
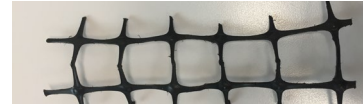
Typical deformed geogrids after test

(a)

Dial gauge

Shearing direction

Load cell

Load plate

Vertical Load

37 mm

Subballast

Clamping blocks

37 mm

Geogrid

200 mm

Electric motor

Subballast

Dial gauge

300 x 300 mm
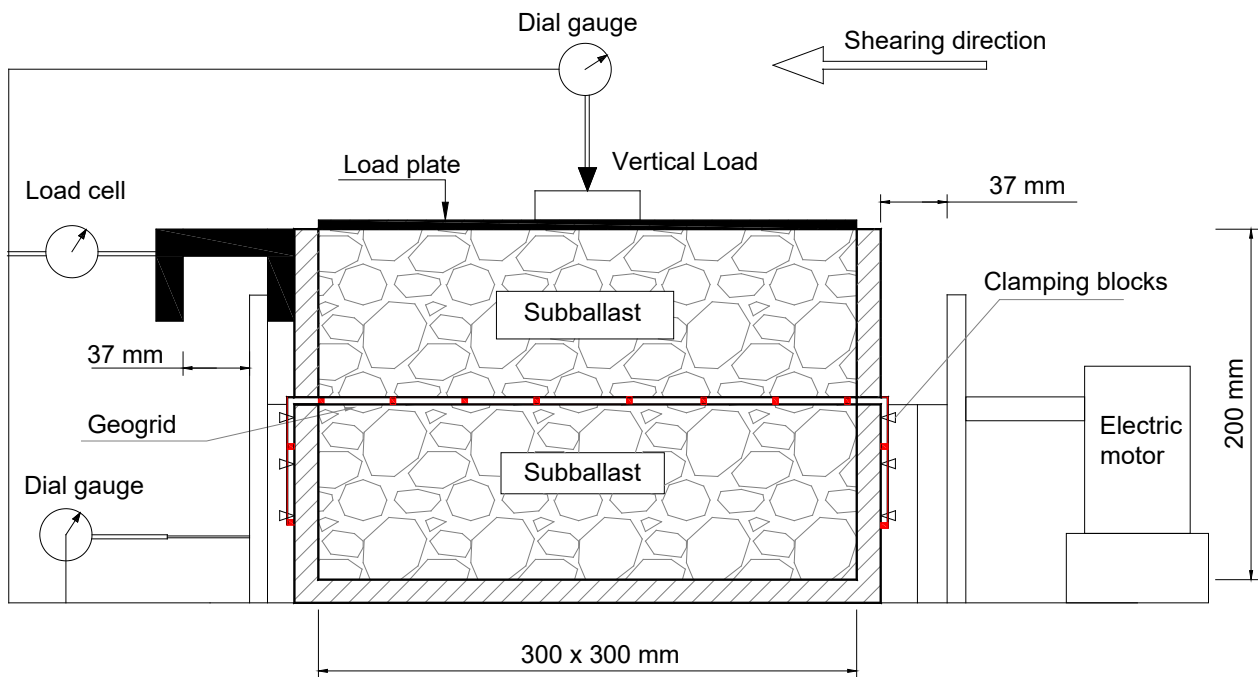
(b)

Fig 2 Large-scale direct shear test for subballast: (a) geogrids used; (b) schematic diagram of the shear box.
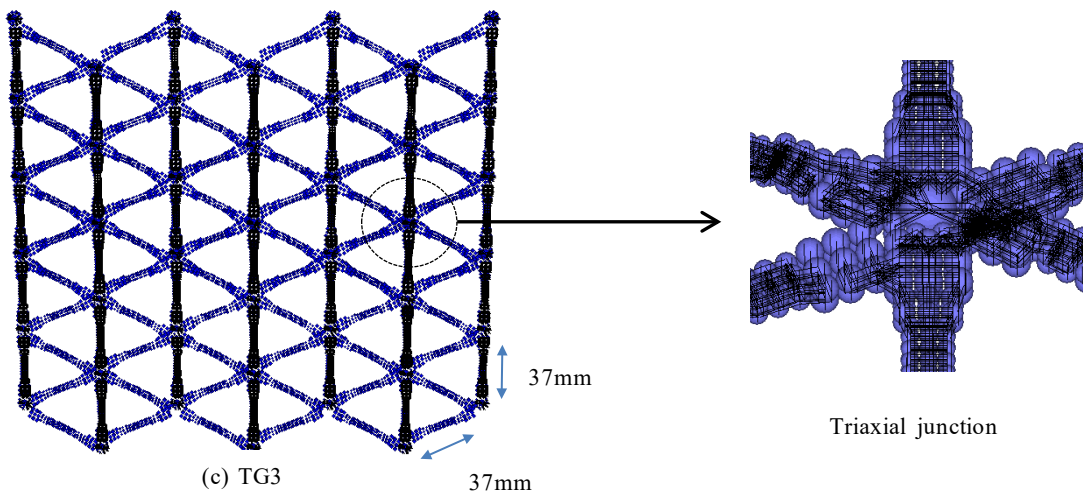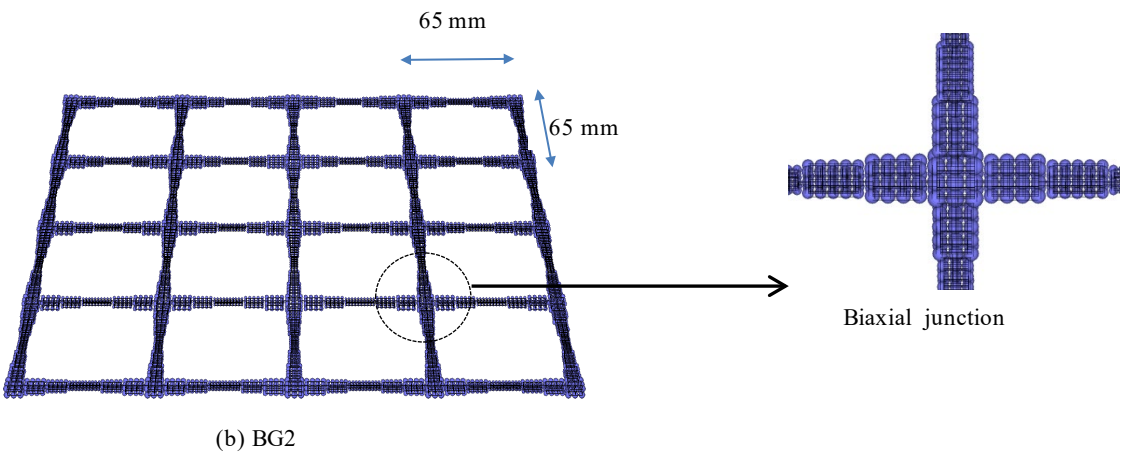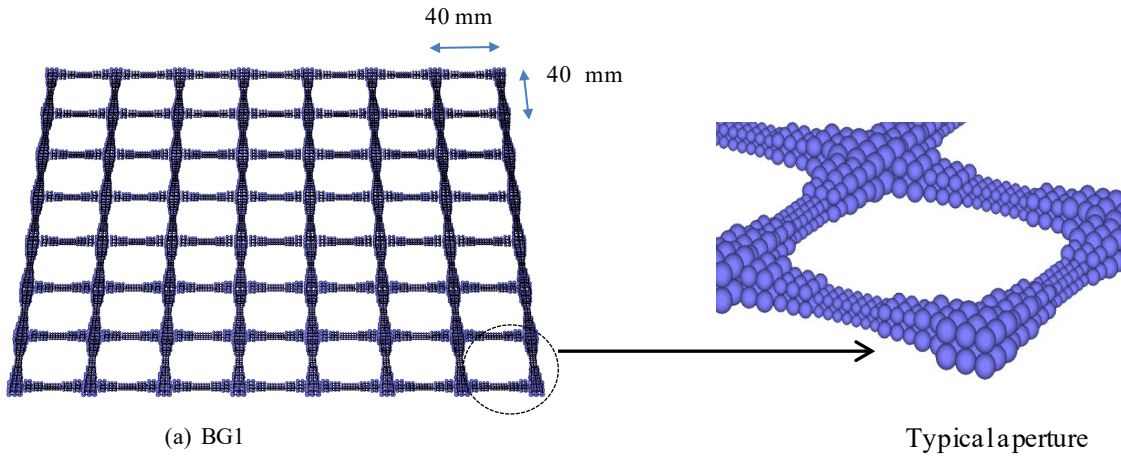
Fig 3 DEM modelling for geogrids: (a) Biaxial grid (BG1: 40 mm × 40 mm); (b) Biaxial grid (BG2: 65 mm × 65 mm); and (c) Triaxial grid (TG3: 37 mm × 37 mm)

(a) Laboratory tensile test

(b) Tensile Load, **P**

DEM simulation

(c)
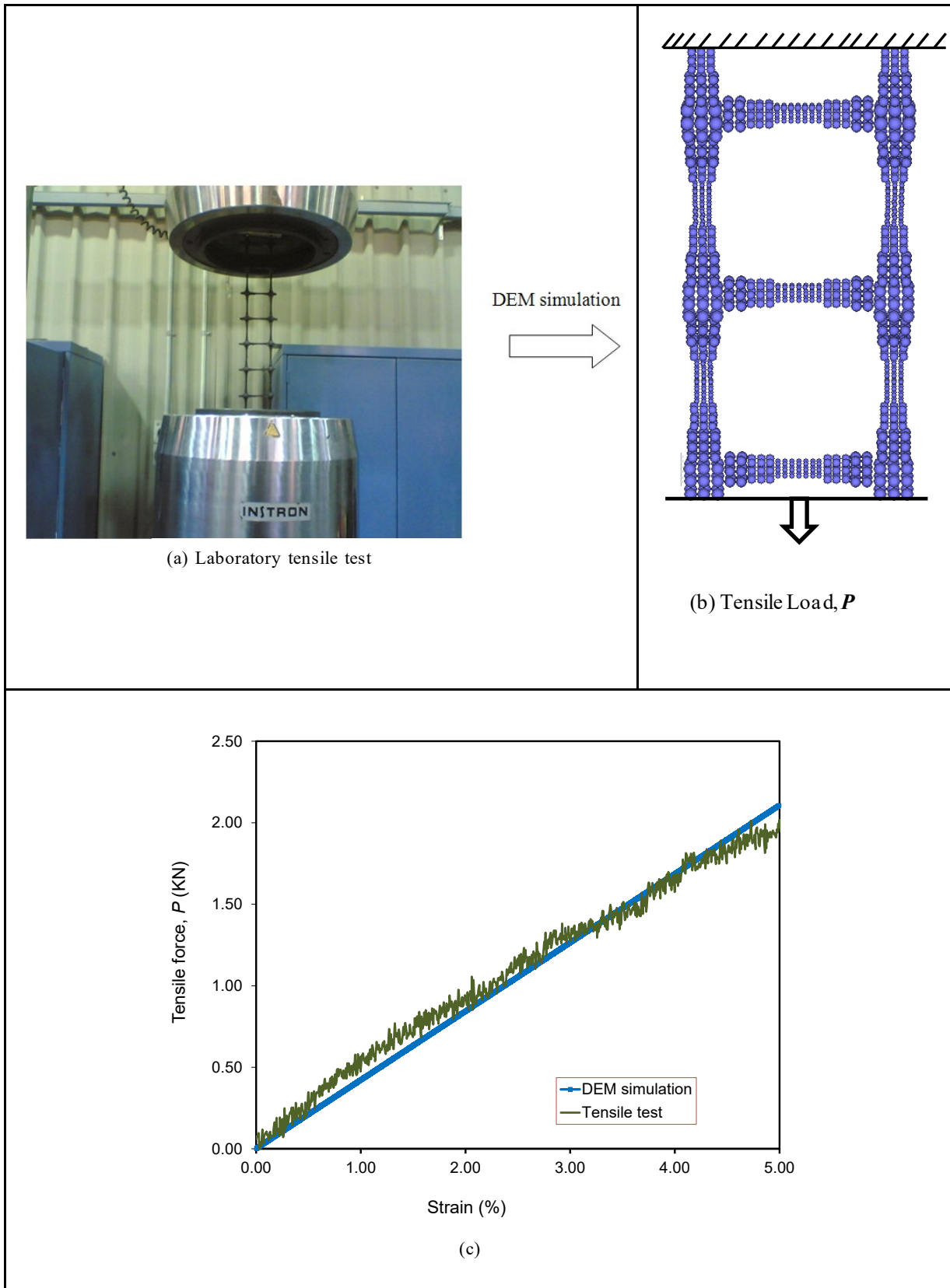
Fig. 4 Calibration of the geogrid: (a) tensile testing for a biaxial geogrid: (b) DEM simulation; and (c) comparison of DEM and experimental data
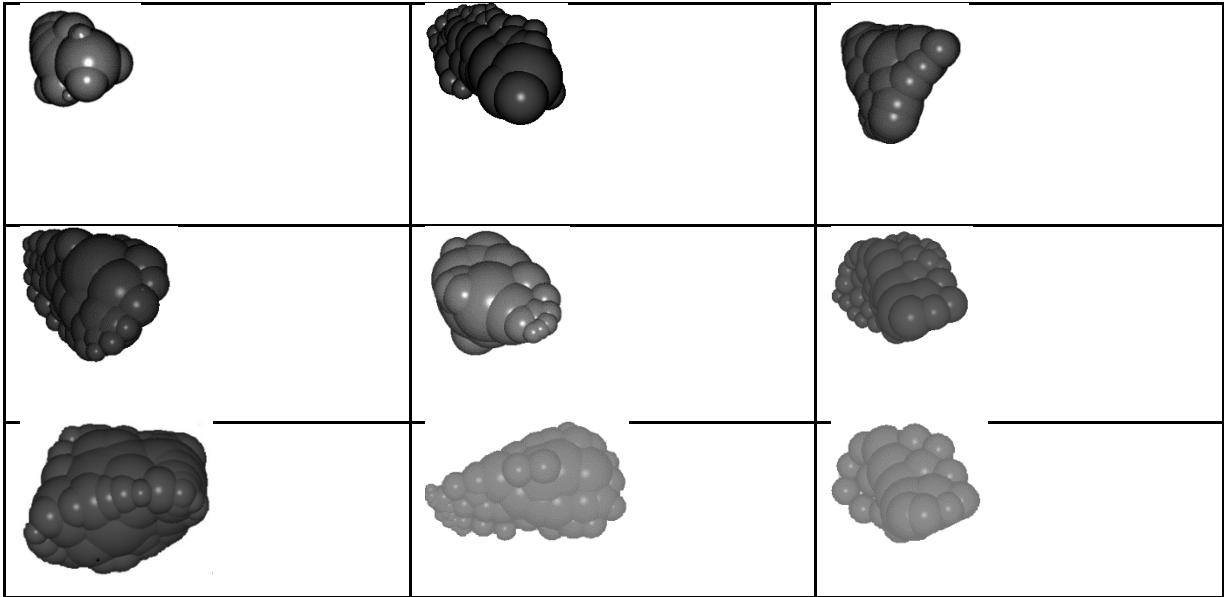
(a)
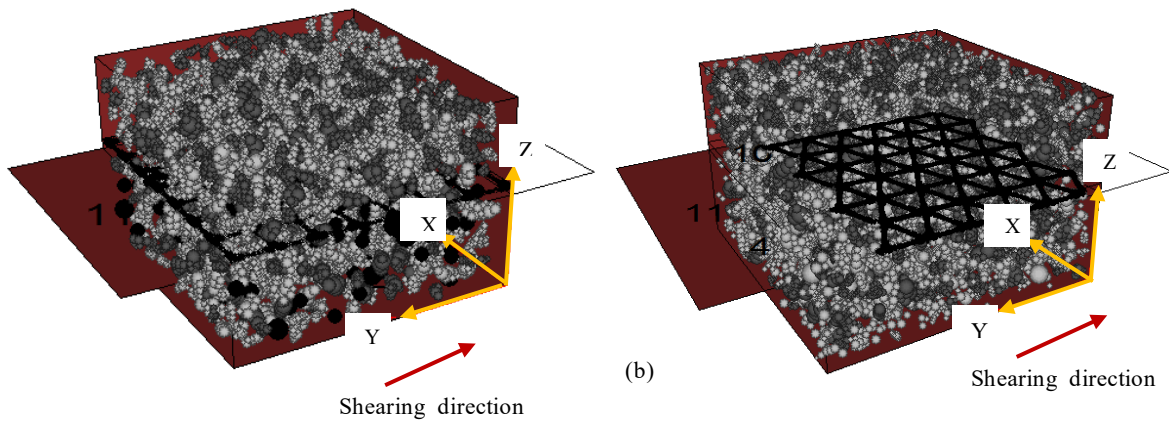
(b)

Fig. 5 DEM modelling of direct shear box: (a) simulated subballast particles; (b) direct shear box with the inclusion of biaxial geogrid (BG1) and triaxial geogrid (TG3)
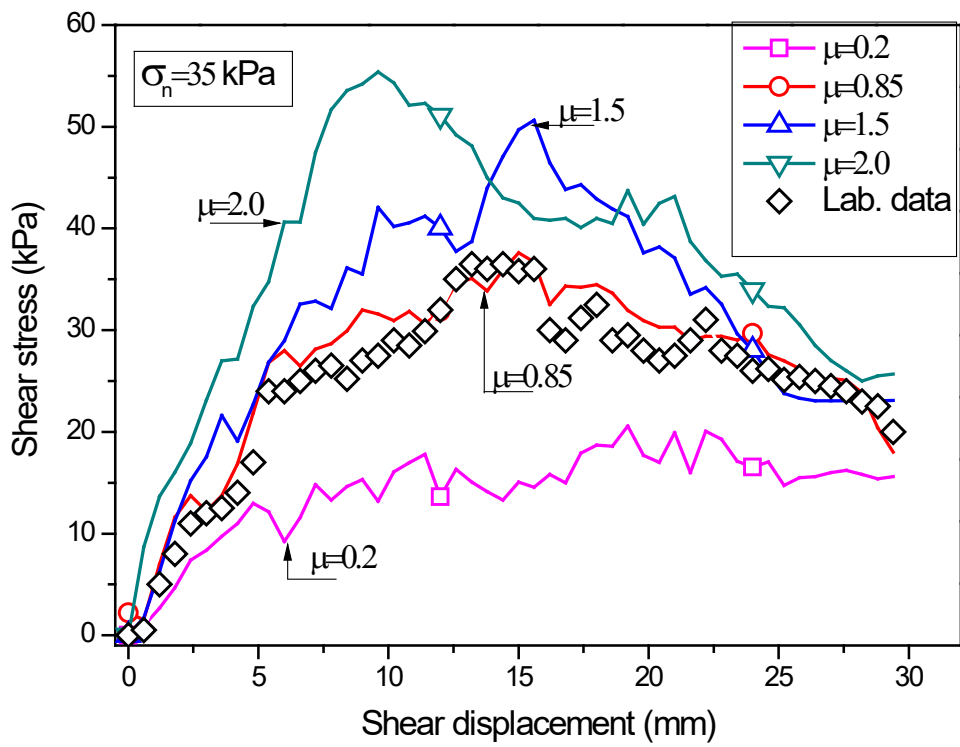
Fig. 6 Parametric study the friction coefficient, μ on the shear stress-displacement response of subballast
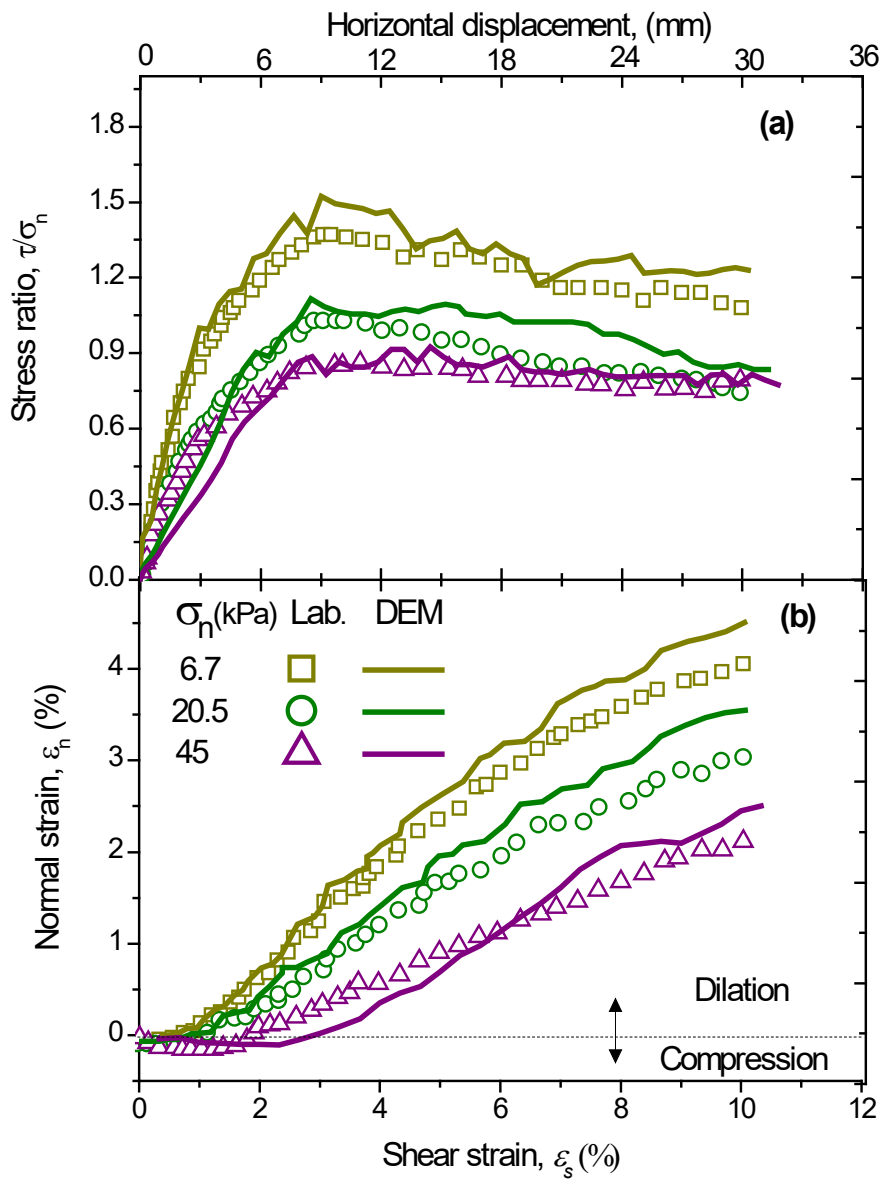
Fig. 7 Comparisons between DEM simulation and experiment for unreinforced subballast at varying normal stresses (a) shear stress ratio versus shear strain, (b) normal strain versus shear strain
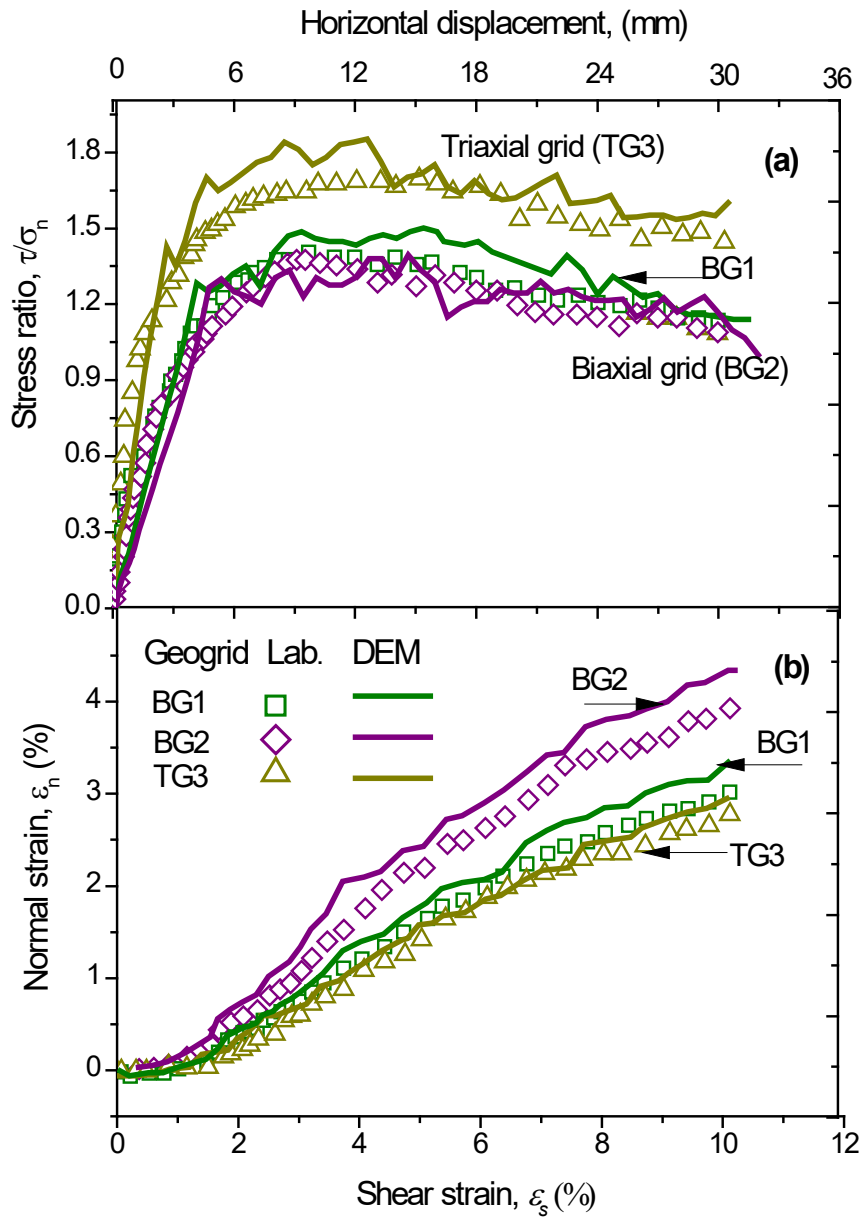
Fig. 8 Comparisons between DEM simulation and experiment for reinforced subballast: (a) shear stress ratio versus shear strain, (b) normal strain versus shear strain
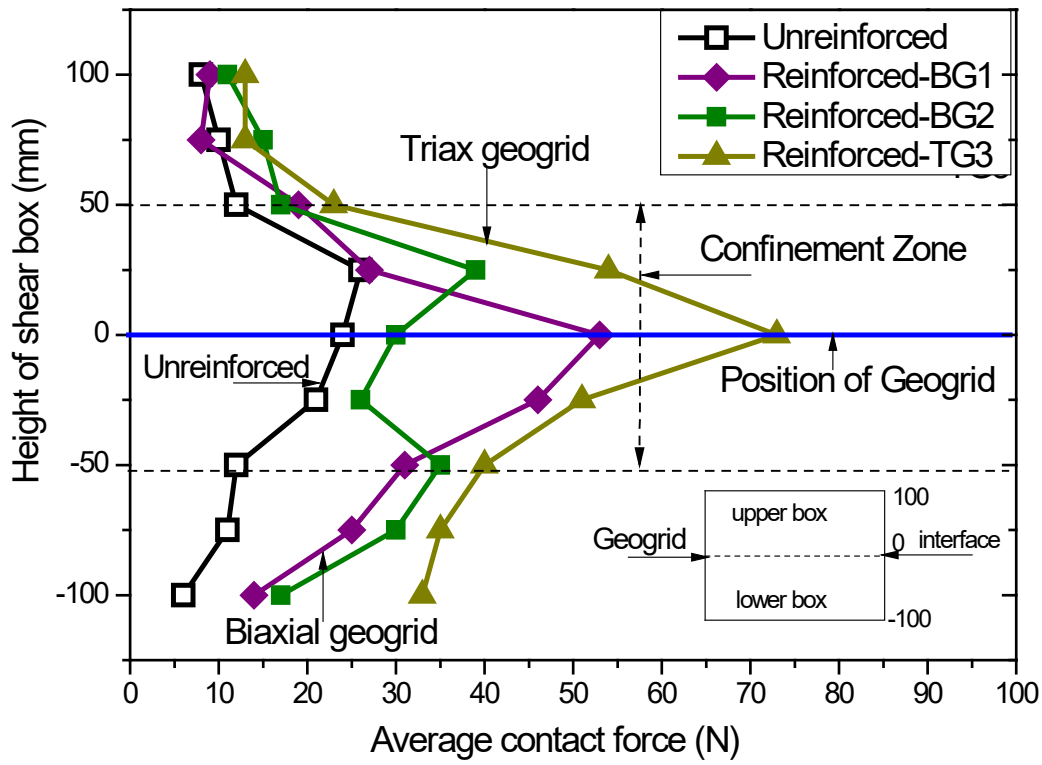
Fig. 9 Average contact force of unreinforced/reinforced subballast specimens subjected to a shear strain of $\varepsilon_s = 5\%$
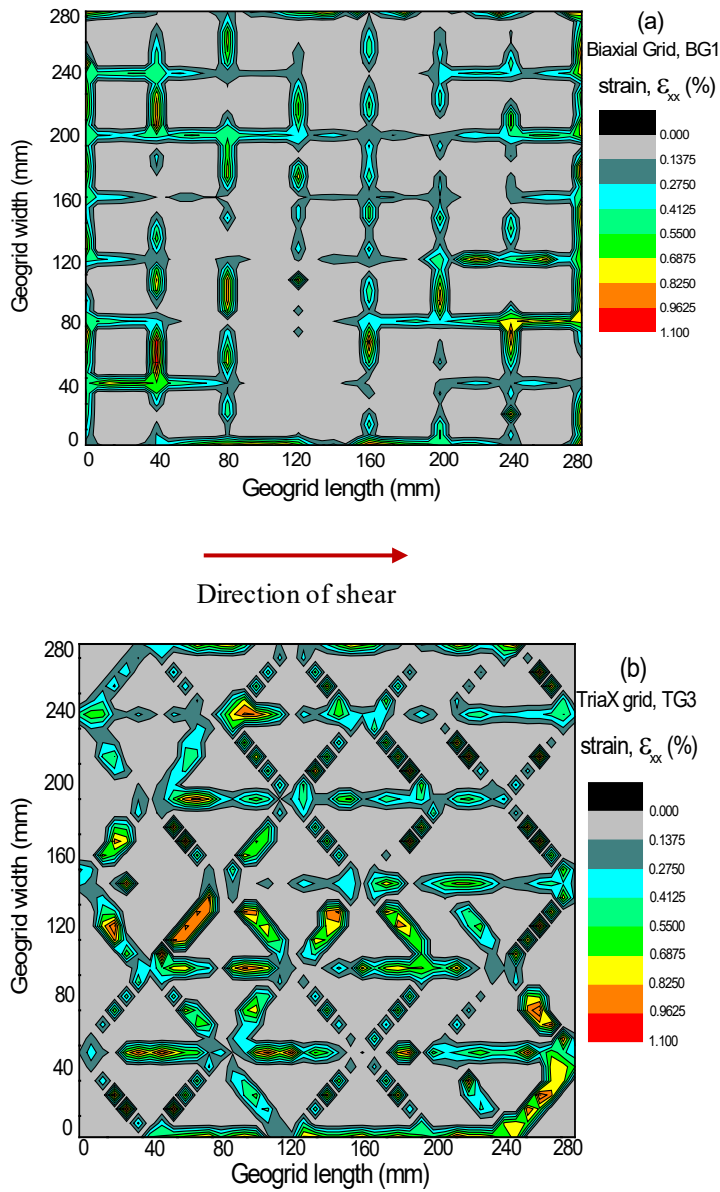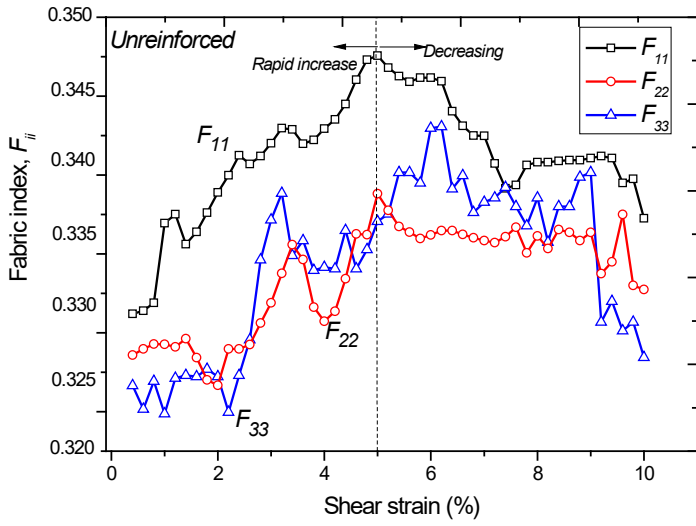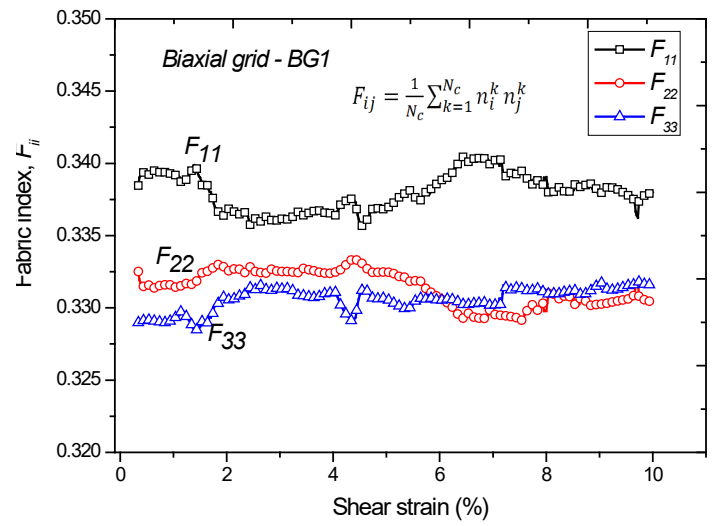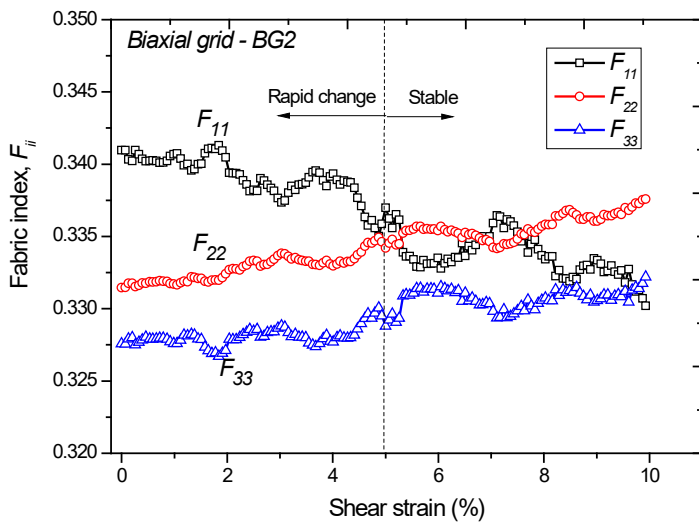
Fig. 10 Contour strains developed across the geogrid in horizontal shearing direction at the shear strain of $\varepsilon_s = 5\%$: (a) biaxial geogrid, BG1; and (b) triaxial geogrid, TG3
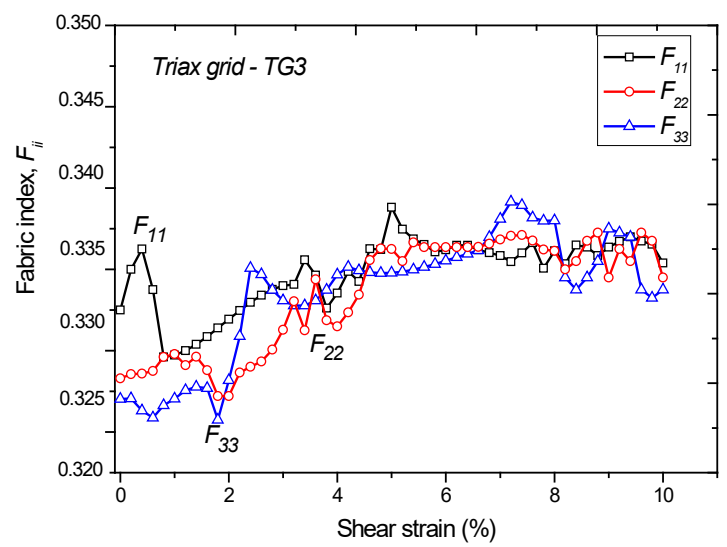
The figure consists of four panels (a), (b), (c), (d) showing plots of Fabric index, F_{ii} versus Shear strain (%).

(a) *Unreinforced*. Annotations: "Rapid increase" and "Decreasing". Legend: F_{11}, F_{22}, F_{33}. Curves labeled F_{11}, F_{22}, F_{33}.

(b) *Biaxial grid - BG1*. Equation: $F_{ij} = \frac{1}{N_c} \sum_{k=1}^{N_c} n_i^k n_j^k$. Legend: F_{11}, F_{22}, F_{33}. Curves labeled F_{11}, F_{22}, F_{33}.

(c) *Biaxial grid - BG2*. Annotations: "Rapid change" and "Stable". Legend: F_{11}, F_{22}, F_{33}. Curves labeled F_{11}, F_{22}, F_{33}.

(d) *Triax grid - TG3*. Legend: F_{11}, F_{22}, F_{33}. Curves labeled F_{11}, F_{22}, F_{33}.

Fig. 11 Evolution of fabric indices of : (a) unreinforced subballast; (b) BG1-reinforced subballast; (c) BG2-reinforced subballast; and (d) TG1-reinforced subballast.
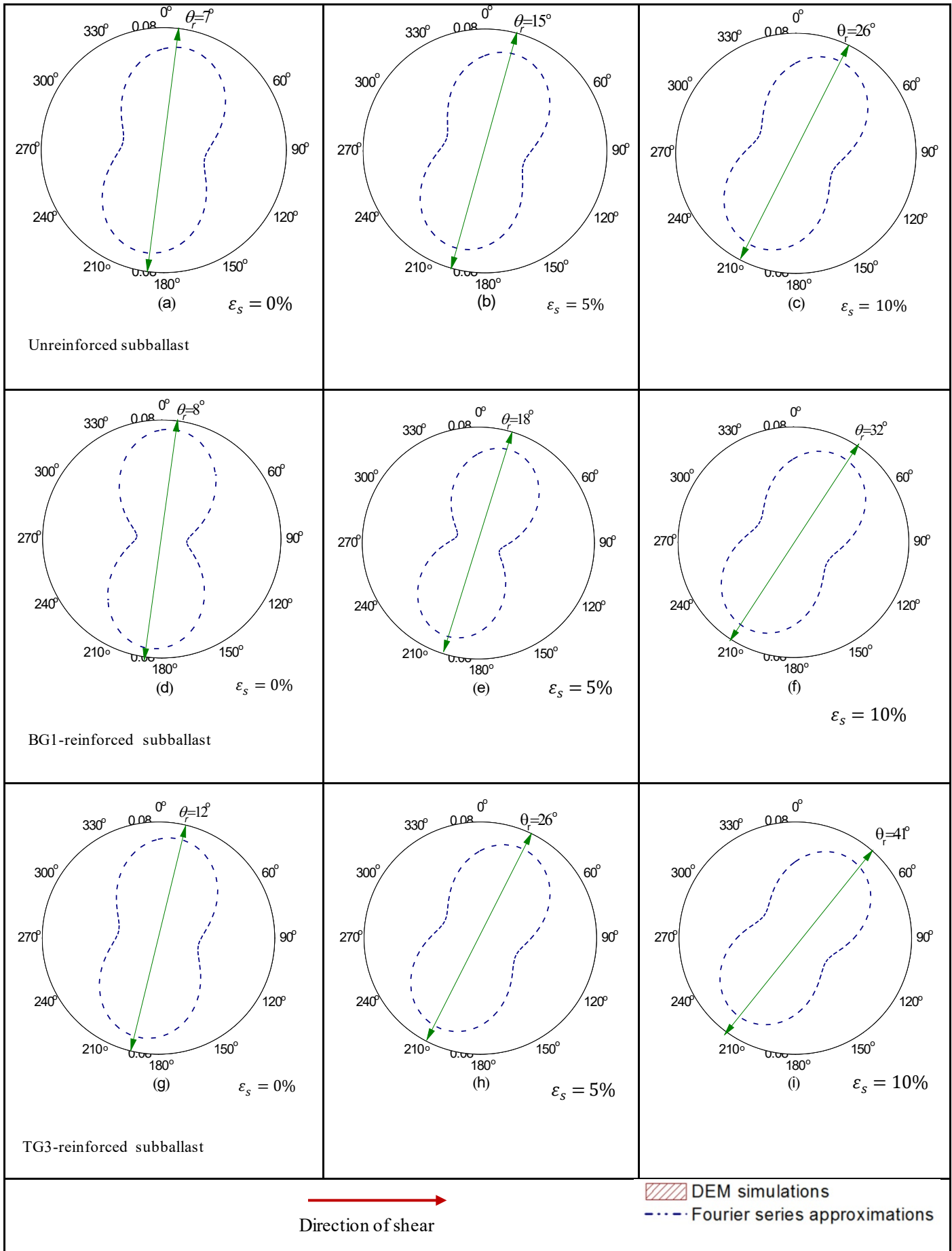
Fig. 12 Polar histogram of contact orientations at different shear strains, $\varepsilon_s = 0, 5, 10\%$: (a-c) unreinforced subballast; (d-f) Biaxial grid, BG1-reinforced; (g-i) Triaxial grid, TG3-reinforced.
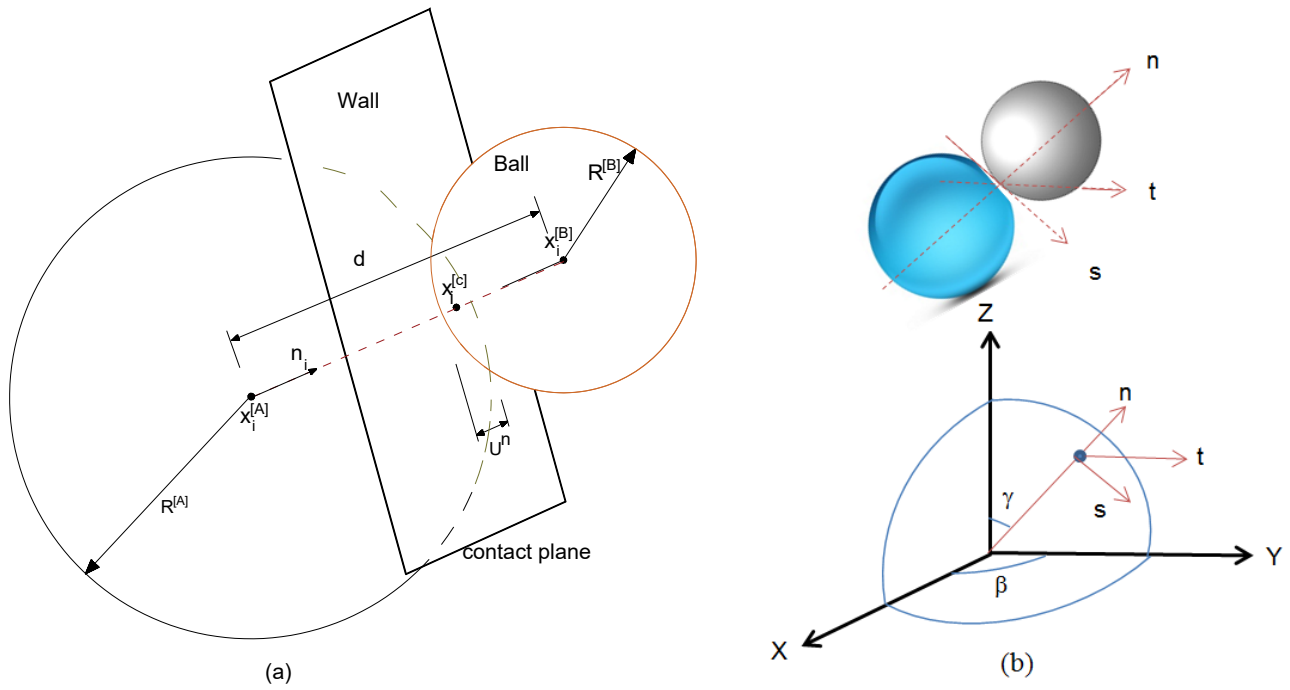
Fig. 13 (a) notation used to describe contacts in DEM; (b) local coordinate at interparticle contact